

# The effect of spontaneous permeation on the interlayer bond strength of 3D printed cement mortars

Yaqing Jiang<sup>a</sup>, Tinghong Pan<sup>a, b\*</sup>, Xuping Ji<sup>a, c\*</sup>

<sup>a</sup> College of Mechanics and Materials, Hohai University, Nanjing 211100, China;

<sup>b</sup> Yunnan Provincial Key Laboratory of Civil Engineering Disaster Prevention, Faculty of Civil Engineering and Mechanics, Kunming University of Science and Technology, Jingming South Road, Kunming, 650500, China;

<sup>c</sup> State Key Laboratory of High Performance Civil Engineering Materials, Jiangsu Sobute New Materials Co. Ltd., Nanjing, 211103, China;

\*corresponding author

E-mail addresses: [thpantt@gmail.com](mailto:thpantt@gmail.com) (T. Pan), [xpji@hhu.edu.cn](mailto:xpji@hhu.edu.cn) (X. Ji).

## Abstract:

The spontaneous permeation of “overlay” is a critical factor affecting the mechanical link of layer-to-layer interfaces. This work mainly studies the possibility of improving the interlayer bonding of 3D printed structures by increasing the spontaneous permeation of “overlay”. A polycarboxylate superplasticizer with high slump retention (TSRS) are employed to control the spontaneous permeation of cement-based materials. The rheological properties, micro-structure and interlayer bonding strength of printed structures with TSRS polymers are analyzed. Results indicate that fluidity is the key factor affecting the spontaneous permeation of cement-based materials. Properly improving the fluidity retention of cement-based

---

\* Corresponding authors.

E-mail addresses: [thpantt@gmail.com](mailto:thpantt@gmail.com) (T. Pan), [xpji@hhu.edu.cn](mailto:xpji@hhu.edu.cn) (X. Ji).

materials can promote the spontaneous permeation of “overlay”, which fills part of the air-void systems of layer-to-layer interfaces, increases the mechanical interlocking and interlayer bonding strength of printed structures.

**Keywords:** Cementitious materials; 3D printing technology; spontaneous permeation; Interlayer bond strength, X-ray micro computed tomography

## 1. Introduction

Intelligent construction is an important development direction of the construction industry in the future. The 3D printing technology for cementitious materials (3DPC) is the core and key to realize intelligent building manufacturing [1-3]. For the construction industry, 3DPC technology breaks through the limitations of the traditional formwork-casting method, and may build structures with complex shapes that cannot be built by the traditional formwork-casting method. Compared with traditional formwork-casting method, 3DPC technology bring significant technological advancements for building-construction industry, such as no needs for formwork [4, 5], reducing design time and execution period reducing labour costs [1, 6, 7], reducing wastes and increasing freeform architectural designs [6, 8]. However, in terms of practical process application, 3DPC technology still suffers many challenges which hinder its applicability as a conventional construction method [9-11].

Layer-to-layer interfaces occurs in the 3D printed structures, due to the inherent “layered” nature, which may be the weakest links in the entire structure. This weakest links may negatively affect the mechanical properties (especially interlayer bonding strength) and the durability of 3D printed structures [12]. The weakest links within interlayer zone of printed structures is one of the limitations of 3DPC technology [10, 11]. The links between adjacent layers can be classified as chemical and mechanical. Chemical link referring to the hydration and bonding of cement particles across the interface. While mechanical link relies solely on the physical attributes of the layers [13].

The mechanical link of layer-to-layer interfaces is mainly contributed by the

mechanical interlocking, which is generated by counterchange between adjacent layers. From the three zones-two layers model, it can be seen that the “overlay” infiltrate into cracks and holes on the surface of the substrate, a permeable layer and reaction layer will be formed at the interface, which are effective for providing mechanical interlock behavior at layer-to-layer interfaces [14]. A thin permeable layer and reaction layer may result in weak adhesion between adjacent layers, while the strengthening of both the permeable layer and the reaction layer may leads to a notable increase in bond strength [14].

The morphological of both the substrate and the “overlay” may affect the mechanical bond between adjacent layers. The increased interface roughness accelerates the mechanical interlock effects [15]. Some surface preparation techniques, such as sand blasting and water jetting are generally used to enhance the mechanical bond of layer-to-layer interfaces [16-22]. In the case of extrusion-based 3D printing technology for cement-based materials, sand blasting is not trivial, due to the high number of layers would unlikely be economical [19]. Zareiyan and Khoshnevis [23] proposes a tongue and groove style layer fabrication (i.e., macroscopic roughness), which increases the contact area and interlocking.

The rheological properties of both the substrate and the “overlay” also significantly affects the mechanical bond between adjacent layers. The fresh cement-based materials with good wettability and spreading can successfully fill and permeate into the pores and cracks in the interface of substrate, thus resulting in an initial formation of mechanical interlock between the two zones [24-26]. While the materials with relatively lower workability can’t penetrate into the roughness profile, therefore exhibits not only poor anchorage but reduced contact area [11, 25, 27]. Taylor et. al. reported that using a paste layer with higher and sustained flow characteristics increases the bond strength of between adjacent layers [11]. The higher flowability of the paste mixtures would successfully fill and permeate into the pores and cracks in the interface of substrate. Vibration may be used to increase the flowability of cement-based materials and to enable physical intermixing of layers.

However, external vibration is risky for the already deposited layers, since it would disrupt the buildability [19].

According to the above description, in order to ensure excellent fusion and bonding between adjacent layers, good wettability and spreadability are needed to ensure that the “overlay” can spontaneously permeate into the surface of substrate and form mechanical interlocking. However, in the 3D printing process of cement-based materials, a high structural build-up is required to ensure the buildability of the printing structures. After the printing filament is extruded, it needs to quickly obtain enough strength to support the self-weight of the printed layer and the gravity of subsequent printed layers. In fact, if the cement-based materials restructure itself too fast (high structural build-up or high thixotropy) may result in the loss of workability and expansibility, and thus affecting the spontaneous permeation of “overlay”. Panda et al. [28] reported that lower thixotropic material is conducive to interlayer bonding. Excessive structural build-up is reported to detrimentally affect the mechanical bond of layer-to-layer interfaces [29-32]. Assaad et. al. [29-32] reported that the materials with moderate thixotropy are best suited for multilayer casting.

This work mainly studies the possibility of improving the interlayer bonding of 3D printing cement-materials by adjusting the rheological properties and increasing the spontaneous permeation of “overlay”, under the premise of ensuring the buildability of the 3D printing cement-based materials. A polycarboxylate superplasticizer with high slump retention (TSRS) are employed to control the spontaneous permeation of cement-based materials. The thixotropic properties, static yield stress and fluidity of cement mortar with TSRS polymer are analyzed by the rheological property test, the micro-structure of printed structures is characterized through X-ray micro computed tomography and the interlayer bonding strength of printed structures are measured by the direct tensile test.

## **2. Spontaneous permeation of cement-based materials**

Spontaneous permeation refers to the process that the upper printing layer migrates downward induced by the gravity or external force to fill the pores and

cracks on the surface of the substrate, as reported in Fig. 2. In 3D printing technology, controlling the permeation of upper layer (or “overlay”) into the lower layer (or substrate) is critical to the bond between adjacent printed layers, which has been frequently studied in selecting binder jetting 3D printing technology [33, 34].

For 3D printable cement mortars, it belongs to Bingham fluid. Meanwhile, the surface of the substrate layer can be regarded as a porous medium composed of multiple small hollow tubes. Therefore, the permeation of upper layer into the lower layer may be considered as the flow of Bingham fluid into multiple pipes. A cylindrical thin layer with radius  $r$  and thickness  $dr$  is isolated in a uniform pipe with diameter  $d$  and length  $l$ . When Bingham fluid undergoes laminar flow, the pressure difference in the thin layer is consistent with the shear force on the slurry.

$$P \cdot \pi r^2 = \tau \cdot 2\pi r l \Rightarrow \tau = \frac{Pr}{2l} \quad (1)$$

where,  $p$  is the pressure difference (Pa),  $v$  velocity (m/s),  $\mu_b$  plastic viscosity and  $\tau$  shear stress.

The rheological equation of Bingham fluid can be expressed as follows:

$$\tau = \tau_0 + \mu_b \frac{dv}{dr} \quad (2)$$

where,  $\tau_0$  is the yield stress of Bingham fluid.

When  $dv/dr=0$ , i.e.  $v=0$ , equation 2 can also be expressed as follows:

$$\tau = \tau_0 = \frac{P_0 r}{2l} \quad (3)$$

where,  $P_0$  is the critical pressure difference while Bingham fluid begins to flow.

$$P_0 = \frac{2\tau_0 l}{r} \quad (4)$$

From above analysis, it can be concluded that there is a critical pressure gradient for the permeation of upper layer into the lower layer, which is proportional to the yield stress of the Bingham fluid. Thus, it may speculate that the yield stress of cement mortar significantly affects the permeability between adjacent printing layers, which is in good agreement with the results obtained by Weger et al. [34]. Thus, we can speculate that the cement mortar with lower growth rate of static yield stress may be better for the 3D printing process.

### **3. Materials & methods**

#### *3.1 Printable mixture design*

Two printable mixtures that were developed by the authors [31] were used in the current study, As shown in Table 1. Ordinary Portland cement (OPC, Type II, 42.5 grade, Nanjing Conch Cement Co. Ltd) was selected as the binder. Attapulgite clay (Jiangsu Jiuchuan Nano-material Technology Co.Ltd.) exfoliated into nanoparticles (called as nano clay, Nc) shaped with 135 nm average length and about 58 nm diameter was selected as the thixotropic admixture [35, 36]. Hydroxy propyl methyl cellulose (HPMC, Renqiu Cheng Yi Chemical Co.Ltd.) was selected as viscosity modifier. The chemical compositions of OPC and Nc were given in Table 2. Except for the type of superplasticizer, both mixture compositions were kept identical, for instance, binder to sand ratio of 1:1.5, water to binder ratio of 0.32, the dosage of Nc, HPMC and superplasticizer were fixed as 0.8 wt%, 0.24 wt% and 0.3 wt% (of the binder mass), respectively. Two types of superplasticizers: a high dispersion polycarboxylate superplasticizer (DPCS), and a polycarboxylate superplasticizer with high thixotropy and high slump retention (TSRS) were employed.

The Fourier transformer infrared spectra (FTIR), Gel permeation chromatography (GPC) and TOC adsorption of DPCS polymer and TSRS polymer were reported in Appendix A, Appendix B and Appendix C.

#### *3.2 Specimen preparation*

JJ-5 planetary cement mortar mixer was used to mixing materials. Firstly, dry batch, such as cement, fine aggregate and nano clay were mechanically mixed for one minute in the cement mortar mixer to form a homogenous mixture. Next, the water and superplasticizer were poured into the mixer and mechanically mixed with dry batch for 60 s at a slow speed. Then stopping for 30 s to scrape off the residual slurry on the wall of the mixer. Lastly, the cement paste was quickly mixed for 90 s. The whole mixing process lasted for 3 minutes, since water was mixed with dry batch. The mixture was immediately placed into a specific container for rheological properties test and poured into 3D printer.

### 3.3 Rheological Measurements

Rheological behavior is one of the most important performance, in the study of 3D printing ink, which play a significant role in describing the pumpability, extrudability and buildability of mixtures [37, 38]. In this work, the rheological properties of mixtures, such as viscosity, yield stress, static yield stress and the area of thixotropic hysteresis loop are characterized using BROOKFIELD RST-SST rheometer. Two rheological testing protocols are proposed to quantitatively measure the area of thixotropic hysteresis loop and static yield stress, respectively.

#### 3.3.1 Thixotropic hysteresis loop

Thixotropic hysteresis loop method is one of the most popular method to evaluate the thixotropy of cement mortar [39], as shown in Fig. 3. The mixtures are first pre-sheared for 120 s by applying a shear rate sweep from 0 1/s to 100 1/s, which is mainly used to create a uniform environment with little test error. Then, after 10 s of rest, an increasing shear rate ramp from 0 1/s to 100 1/s within 100 s is applied to produce the up-curve of the flow test. Finally, the shear rate decreases from 100 1/s to 0 1/s within 100 s to obtain the down-curve of the flow test. The up-curve and down-curve of the flow test form the envelope region of hysteresis loop, as shown in Fig. 3(b). The area of thixotropic hysteresis loop is related to the energy needed to destroy the flocculation structure, which can be expressed by Equation (5).

$$A = \int_{\dot{\gamma}_{min}}^{\dot{\gamma}_{max}} \tau_1 \dot{\gamma} d\dot{\gamma} - \int_{\dot{\gamma}_{min}}^{\dot{\gamma}_{max}} \tau_2 \dot{\gamma} d\dot{\gamma} \quad (5)$$

where,  $A$  is the area of thixotropic hysteresis loop,  $\dot{\gamma}$  the shear rate (1/s),  $\tau_1$  and  $\tau_2$  the maximum and minimum value of the shear stress, respectively.

#### 3.3.2 Static yield stress

This protocol is used to monitor the development of static yield stress with resting time. After mixing, mixture was divided into 10 groups to measure the value of static yield stress at different resting time. 10 groups of samples are put into different glass bottles, and then each group is manually stirred for 1 minute to ensure that all samples have the same initial structure. After resting for a certain time (0 s,

150 s, 300 s, 450 s, 600 s, 750 s, 900 s, 1050 s, 2000 s and 3000 s, respectively), the sample is taken out to test the static yield stress, as shown in Fig. 4(a). In the static yield stress test protocol, a constant shear rate of 0.02 1/s is used. The maximum shear stress on the shear stress vs time curve is defined as static yield stress [40], as shown in Fig. 4(b). According to the research results of Ivanova and Yuan et al. [41, 42], the development of static yield stress can be used to monitor the structural build-up of cement-based materials.

### *3.4 Printing device and printing parameters*

A self-made laboratory level gantry 3D printer with forming space of 500 mm × 500 mm × 500 mm is used with a screw extrusion, as shown in Fig. 5. A square nozzle with opening of 40 mm × 20 mm is used in this work, which results in a large surface contact area between the adjacent extruded layers. The moving speed  $v$  of nozzle is set as 60 mm/s and the height  $h$  between the nozzle and the build surface is fixed at 25 mm. The screw rod driven by stepper motor is used to extrude the 3D printed ink out of a nozzle and the extrusion rate  $E$  is set as 12 mL/s, by adjusting the rotation rate of screw rod.

Double-layer structures with different types of superplasticizers and different printing time interval are prepared for the interlayer bonding strength test and X-CT test, as shown in Table 3. The actual printed results are reported in Fig. 6. After double-layer structure is printed, the strip sample is cut into small squares with a length of 40 mm, immediately. Then the cut specimen is cured in the standard curing environment for 28 days.

### *3.5 X-ray computed tomography*

#### *3.5.1 X-CT image acquisition and segmentation*

Microstructure of printed structures are performed using a Nikon metrology x-ray CT computed tomography (Nikon XTH) system supplied form Nikon metrology instruments.

#### *3.5.2 Air void characterization*

In this work, the plane porosity and fractal dimension of 2D slice that perpendicular to the stacking direction of the printed layer are used to quantitatively characterize the pore characteristics within the interlayer zone of 3D printed cement mortars. Porosity can directly reflect the compactness of the printed structures, and can be obtained from the proportion of pore area in the total area of 2D slice, as shown in Fig. 7.

$$\phi = \frac{A_V}{A_T} \quad (6)$$

where  $\phi$  is the plane porosity,  $A_V$  the area of void space in 2D slice,  $A_T$  the total area of 2D slice.

Fractal dimension can characterize the complexity of structure from a multi-scale perspective [43]. Mandelbrot [44] has pointed out that fractal dimension provides a new approach to describe the self-similarity and complexity of objects. Many calculation methods, such as box-counting dimension, triangulation and power spectrum, have been used to characterize the fractal characteristics of structures [45]. In this work, box-counting dimension is used to evaluate the fractal characteristics of pores in 2D slices. For complex structures with autocorrelation, the box-counting dimension  $D^b$  can be expressed as:

$$D^b = \log(N^k)/\log(1/k) \quad (7)$$

where  $N^k$  is the minimum number of grids that covering the surface of complex structure with square grid with side length  $k$ . Box-counting dimension indicates that the number of square grids  $N^k$  increases with the decrease of side length  $k$ , and the calculation algorithm of box-counting dimension on 2D slice is shown in Fig. 7.

### 3.6 Interlayer bonding strength

Before the tensile loading test, the upper and lower ends of the specimen have been cut and polished, and the total thickness of the specimen after polishing is about 20 mm. Then, the samples are bonded to the molds with high-strength epoxy glue, as shown in Fig. 8. In the tensile bond strength testing, tensile loading at a loading speed of  $0.035 \pm 0.015$  MPa/s is applied to both the upper and lower ends of specimen. The tensile bond strength is calculated through the ratio of maximum tensile force to

effective bonding area.

## 4. Results and discussion

### 4.1 Rheological properties of cement mortars

The test results of thixotropic hysteresis loop, fluidity of mortar and static yield stress are shown in Fig. 9(a, b, d). In the up-curve of the thixotropic hysteresis loop testing protocols, there are more flocculation structures in the cement suspension, which increases the shear resistance of the rotor, and results in a higher shear stress [46]. In the down-curve of the thixotropic hysteresis loop testing protocols, part of the flocculation structure is destroyed, which decreases the shear resistance of the rotor and results in a lower shear stress than that in the up-curve [46]. The difference between the up-curve and down-curve is attributed to the content of flocculation structures in the cement suspension. Compared with DPCS polymer, TSRS polymer significantly increases the thixotropic hysteresis loop area of cement mortar, as shown in Fig. 9(a), which indicates that there are more (about twice) flocculation structures in the cement suspension with TSRS than that with DPCS.

Fig. 9(b) shows the initial fluidity of cement mortar with DPCS polymer is higher than that with TSRS polymer, which indicates that the DPCS polymer has better dispersion performance. However, the fluidity loss of cement mortar with DPCS polymer is higher than that with TSRS polymer, which indicates that the TSRS polymer has better slump-retention performance.

Fig. 9(d) reports the time-varying curve of static yield stress, which can be fitted by a nonlinear equation [31], and the fitted results are summarized in Table 4. The TSRS polymer improves the short-term structural build-up rate  $R_{thix}$ , but it significantly decreases the long-term structural build-up rate  $A_{thix}$ . This means that TSRS polymer promotes the physical flocculation. It is worth mentioning that the short-term structural build-up rate  $R_{thix}$  has same trend with the thixotropy represented by thixotropic hysteresis loop, which indicates that  $R_{thix}$  is a better indicator of appropriate thixotropic behaviour for cement mortars than  $A_{thix}$ . This is consistent with the research results of Kruger. et al [49].

The difference of rheological properties between DPCS polymer and TSRS polymer may be attributed to the difference of their molecular structure and adsorption capacity, as reported in Appendix C. The adsorption capacity of cement to the DPCS polymer is higher than that of TSRS polymer at 10 min, which results in a significant steric hindrance effect, helps to destroy the flocculation structure. This may explain the higher flowability and smaller thixotropic hysteresis loop area of cement mixture with DPCS polymer at the initial stage [50, 51]. Then, with the cement hydration, the DPCS molecules adsorbed on the surface particles are continuously consumed, due to the deposition of hydration products (such as Aft and C-S-H, etc.) on the surface of cement particles, which decreases the number of PCs molecules in solution and decreases the adsorption capacity of cement to the DPCS polymer. This may be used to explain why the cement mortar with DPCS has higher fluidity loss and higher construction rate. Conversely, with the hydration of cement, more TSRS molecules would be released into the solution due to the hydrolysis of acrylamide in alkaline environment, which increases the number of PCs molecules in solution and increases the adsorption capacity of cement to the TSRS polymer. This explains why the fluidity-retention ability of the TSRS polymer is better than that of DPCS polymer.

#### *4.2 Air-void systems within the interlayer zone*

##### *4.2.1 Air void content and distribution*

The cement-based materials with different rheological properties may lead to various permeation behaviour at layer-to-layer interfaces, which would significantly affect the micro-structure of printed structures. In this work, plane porosity  $\phi$  is used to characterize local air-void systems of 3D printed structures, the fractal dimension  $D^b$  is used to describe the complexity and irregularity of air-void systems [52]. Fig. 10 and Fig. 11 show how the plane porosity  $\phi$  and the fractal dimension  $D^b$  change along the thickness of printed structures, respectively. These values are obtained through digital image processing technology, as described in section 3.5.2 and the mean values and standard deviations are also calculated.

The plane porosity in the middle-zone of the printed structures is higher than in other areas, which is due to the lack of fusion between the adjacent extruded layers. Based on the stabilization of the average plane porosity, where the interlayer zone begins and finishes is decided, as reported in Fig. 10. Expanding the time interval between adjacent printed layers may lead to a higher concentration of air-void systems in the interlayer zone, which would increase the average plane porosity in the interlayer zone and the thickness of the interlayer zone. Extending time interval may also introduce the ‘wide’ macropores at the interlayer zone. Many ‘wide’ macropores concentrates in the interlayer zone may increase the complexity and irregularity of the air-void systems, which is a possible reason for the increasement of average fractal dimension of the air-void systems in the interlayer zone with the expand of time interval.

Furthermore, the printed structures with TSRS polymer have lower plane porosity and fractal dimension in the interlayer zone than that with DPCS polymer, which may be explained by the higher workability-retention of TSRS polymer. As described in section 2, higher fluidity-retention may promote the spontaneous permeation of upper layer into the surface of substrate, which fills the pores and cracks and resulting in an initial formation of mechanical interlock at layer-to-layer interfaces.

Fig. 12 shows the reconstruction of 3D microstructure of double-layer printed structures based on the CT slice image using X-CT test. Qualitative visual assessing these 3D models, it can be noted that there is a significantly interlayer zone between 1st layer and 2st layer, and the 1st layer, 2st layer and interlayer zone contains the microstructure with a significantly different size, number and space distribution of pores. Many unfilled areas and ‘wide’ macropores are concentrated on the interlayer zone of printed structures, which provides a channel for chloride or carbon dioxide ions ingress and is the possible reason for the weak interlayer bonging strength and bad durability properties of printed structures [53].

#### *4.2.2 Maximum value of plane porosity and fractal dimension*

The maximum value of plane porosity  $\phi_{max}$  and fractal dimension  $D^b_{max}$  in the interlayer zone is therefore investigated and plotted in Fig. 13. Both of time interval and rheological properties significantly affect the maximum value of plane porosity  $\phi_{max}$  and fractal dimension  $D^b_{max}$  in the interlayer zone.

As shown in Fig. 13(b, c), both of the value of  $\phi_{max}$  and  $D^b_{max}$  in the interlayer zone increases with the extend of time interval, which is in good agreement with the results obtained by Yu et al. [54]. For a short-time interval (20 s in this work), the rough surface of 1st layer (substrate layer) may be successfully filled by the spontaneous permeation of “overlay”, which may increase the contact behaviour between the adjacent extruded layers and decreases the porosity in the interlayer zone. For a long-time interval (30 min and 60 min in this work), the substrate layer with poor surface moisture would absorbs water from the newly deposited upper layer [55, 56], which may force more air-void from the substrate layer to the interlayer zone. Furthermore, extending the time interval would increase the stiffness difference and the difference of relative shrinkage between adjacent printing layers, which may result in shrinkage cracks at the interlayer zone [57, 58]. The spontaneous permeation of “overlay” is not enough to fill the increasing air-void systems within the interlayer zone. Thus, the value of  $\phi_{max}$  and  $D^b_{max}$  in the interlayer zone increases with the extend of time interval.

In general, the mixture with TSRS polymer obtains better filling effect, due to higher fluidity-retention may promote the spontaneous permeation of upper layer into the surface of substrate. Although increasing the spontaneous permeation of “overlay” cannot completely eliminate the air-void systems within the interlayer zone, it shows a positive effect for the fusion between adjacent printed layers. For the long-time interval, preventing the surface water evaporates and the formation of drying shrinkage are critical as increasing the spontaneous permeation of “overlay”, and the printing environment may be a key factor affecting the interlayer bond strength [19, 59, 60].

### *4.3 Interlayer bonding strength*

Table 5 summarizes the interlayer bonding strength of 3D printed structures using uniaxial tensile test. Their statistical characteristics, such as mean value ( $\bar{f}_b$ ), standard deviation  $\sigma$  and coefficient of variation  $c_v$  are also marked from three test results.

From table 5, the interlayer bond strength of printed structures with time interval of 20 s is biggest. They are 1.76 MPa and 1.94 MPa for the printed structures with DPCS polymer and TSRS polymer, respectively. Extending the time interval would significantly decrease the interlayer bond strength. For the printed structures with DPCS polymer, the interlayer bond strength of printed structures with time interval of 30 min and 60 min are lower 56.8 % and 77.8 % than that with time interval of 20 s, respectively. For the printed structures with TSRS polymer, the interlayer bond strength of printed structures with time interval of 30 min and 60 min are lower 50.5 % and 75.3 % than that with time interval of 20 s, respectively.

Furthermore, it can be found that the printed structures with TSRS polymer always have higher interlayer bond strength than that with DPCS polymer. For time interval of 20 s, the interlayer bond strength of printed structure with TSRS polymer is higher 10.2 % than that with DPCS polymer. For time interval of 30 min, the interlayer bond strength of printed structure with TSRS polymer is higher 24.7 % than that with DPCS polymer. For time interval of 60 min, the interlayer bond strength of printed structure with TSRS polymer is higher 41.0 % than that with DPCS polymer. TSRS polymer has higher fluidity-retention and workability-retention, which may decrease the stiffness difference between two layers and promote the spontaneous permeation of “overlay”. This is a possible reason for the higher interlayer bond strength of printed structures with TSRS polymer.

As described in section 4.2.2, the mixtures with higher fluidity-retention have better filling effect for the air-void systems of layer-to-layer interfaces, which increases the mechanical interlocking and contact area between adjacent layers. Although the spontaneous permeation of “overlay” cannot completely eliminate the negative effects caused by extending the time interval, it has a position effect on the connect and bond between adjacent layers.

For a quasi-brittle 3D printed cement mortar, the interlayer bonding strength is closely related to the air-void systems within the interlayer zone [54, 61]. Fig. 14 shows the relations between the average plane porosity  $\phi$ , average fractal dimension  $D^b$ , maximum plane porosity  $\phi_{max}$ , maximum fractal dimension  $D^b_{max}$  and the interlayer bonding strength of 3D printed structures, respectively.

As shown in Fig. 14, the value of  $\phi_{max}$  and  $D^b_{max}$  are significantly related to the interlayer bonding strength, while the average plane porosity and average fractal dimension are weakly related to the interlayer bonding strength of 3D printed structures. Compared to the average value of plane porosity and fractal dimension, the maximum value of plane porosity and fractal dimension between the adjacent extruded layers seems to be a more critical factor to dominate the interlayer bonding strength, which is in good agreement with the results obtained by Lee et al. [62]. According to the principle of minimum energy consumption of fracture mechanics, the crack propagation path always follows the surface with the weakest bonding force [63]. Due to the weak adhesive of printed structures mainly concentrated on the interlayer zone, the microcracks propagates mainly along the interlayer zone in the tensile process, especially in the slice with the maximum plane porosity. Thus, the value of  $\phi_{max}$  and  $D^b_{max}$  of interlayer zone are significantly related to the interlayer bond strength. From Fig. 14, it can be found that the average plane porosity and average fractal dimension of 1st layer or 2st layer are not significantly related to the interlayer bond strength, indicating that the microcracks propagates mainly along the interlayer zone may suffer little influence by the microstructure of 1st layer or 2st layer.

## 5. Conclusions

In this work, A polycarboxylate superplasticizer with high slump retention (TSRS) are employed to control the spontaneous permeation of cement-based materials. The effect of spontaneous permeation on the micro-structure and interlayer bonding strength are studied through X-ray micro computed tomography and direct tensile test. The correlation between microstructure and macro interlayer bond

strength of 3D printed structures are established. The following results are obtained:

(1) Fluidity retention is the key factor affecting the spontaneous permeation of cement-based materials. The higher fluidity retention increases the spontaneous permeation of mixture, which results in a lower average plane porosity  $\phi$  at the layer-to-layer interfaces.

(2) The spontaneous permeation of cement-based materials is a critical factor affecting the fusion between adjacent printed layers. On the premise of ensuring the buildability of 3D printed structures, properly improving the fluidity retention of cement-based materials can promote the spontaneous permeation of “overlay”, which fills part of the air-void systems of layer-to-layer interfaces, increases the mechanical interlocking and interlayer bonding strength of printed structures.

(3) The plane porosity and fractal dimension of air-void systems in the interlayer zone are obviously larger than those in the 1st layer or 2nd layer, which may be a possible reason for the weak interlayer bond strength of 3D printed structures. The average plane porosity, the maximum plane porosity and the average fractal dimension of the interlayer zone are linearly related to the interlayer bond strength.

(4) The positive effect due to the spontaneous permeation of “overlay” is opposite to the negative effect caused by extending the time interval. However, only improving the spontaneous permeation of “overlay” is difficult to eliminate the negative effect. The measure that improving the spontaneous permeation of “overlay” is recommended to be combined with other enhancement step.

#### **Appendix A: Fourier transformer infrared spectra (FTIR) measure**

The high dispersion polycarboxylate superplasticizer (DPCS), and the polycarboxylate superplasticizer with high thixotropy and high slump retention (TSRS) were pressed disc with KBr to obtain FTIR data. The wavenumber in the range of 4000-400  $\text{cm}^{-1}$  are recorded on Thermo Scientific Nicolet iS5.

FTIR spectra of DPCS and TSRS are reported in Fig. A1. The peak at about 3428  $\text{cm}^{-1}$  is the stretching vibration peak of hydroxyl (-OH), the peak at about 2875  $\text{cm}^{-1}$  is the characteristic vibrational absorption peak of C-H. The stretching vibration

absorption peak of carboxyl at  $1730\text{ cm}^{-1}$ , the peak at about  $1460\text{ cm}^{-1}$  is corresponding to the C-H bending vibration absorption peak of methylene ( $-\text{CH}_2-$ ), the peak at about  $1345\text{ cm}^{-1}$  is corresponding to the -OH bending vibration absorption peak of carboxyl, the peak at about  $1110\text{ cm}^{-1}$  and  $948\text{ cm}^{-1}$  are corresponding to the C-O-C bending vibration absorption peak, and the peak at about  $845\text{ cm}^{-1}$  corresponding to the  $-\text{CH}_2-$  bending vibration absorption peak. The FTIR results shows that the molecular structures of DPCS and TSRS polymers contain hydroxyl, carboxyl, ether, and other functional groups. In addition, from the FTIR spectra of TSRS, it can be found that there is a significant peak at about  $1580\text{ cm}^{-1}$ , which may be the characteristic absorption peak of  $-\text{NH}_2$ , indicates that acrylamide is introduced into TSRS polymers. This may be a possible reason for the high slump retention of TSRS polymers.

#### **Appendix B: Gel Permeation Chromatography (GPC) measure**

The polymer molecules can be separated by the gel permeation chromatography (GPC), due to their hydrodynamic volume of the polymer molecular is different. The molecular parameters of DPCS polymer and TSRS polymer are evaluated by weight-average molecular weight (Mw), the number-average molecular weight (Mn), the polydispersity index (PD: Mw/Mn). A gel permeation chromatograph (GPC) apparatus (PL-GPC50; PL-GPC220; Waters GPC 1515) is employed to determine Mw, Mn of SAF SP. In this work, 0.10 mol/L sodium nitrate solution (pH of the solution adjusted to 12 with NaOH) as carrying phase at a flow rate of 0.8 mL/min, the mono-dispersive sodium polyethylene sulfonate as the standard phase of calibration.

The molecular weight distribution is one of the most basic structural parameters of superplasticizers. For the polymers with lower molecular weight, it may obtain a shorter molecular chain, which may influence the slump-retention property; for the polymers with higher molecular weight, it may result in the bypass effect, influence the disperse effect of superplasticizers. The high dispersion polycarboxylate superplasticizer (DPCS) and the polycarboxylate superplasticizer with high thixotropy and high slump retention (TSRS) are analyzed by GPC, as shown in Fig. B1.

The weight-average molecular weight and number-average molecular weights of DPCS polymer are 38993 g/mol and 19930 g/mol, respectively. The weight-average molecular weight and number-average molecular weights of TSRS polymer are 15373 g/mol and 7362 g/mol in peak 1, respectively. GPC results shows that the monomer conversion rate is higher in the polymerization of DPCS polymer.

### **Appendix C: TOC adsorption measure**

ET1020A Total organic Carbon (TOC) analyzer produced by Shanghai Euro Tech Ltd. is used to measure the adsorption amount of superplasticizer on the surface of cement particles. Two grams of PCs (DPCS polymer and TSRS polymer) with different concentrations (0.2, 0.4, 0.8, 1.2 and 1.6 g/L, respectively) are prepared. 5g cement powder is weighed and added into PCs solutions with different types and different concentration, respectively. All these mixtures are stirred with a glass rod for 5min, stood for 5min, centrifuged in a centrifuge for 20 min. The filtered solution was taken for total organic carbon analysis. The testing range is from 4 ppb to 4000 ppm. The adsorption capacity is tested at 10 min and 60 min respectively.

The adsorption capacity of the DPCS polymer and TSRS polymer at different concentrations on the surface of cement particles is studied. The adsorption curve is reported in Fig. C1. With the increases of the concentration of the superplasticizer, the adsorption capacity of cement particles to PCs is gradually increasing. The adsorption capacity of cement to the DPCS polymer is higher than that of TSRS polymer at 10 min, which may explain the higher flowability of cement mixture with DPCS polymer at the initial stage. Then, with the hydration of cement, the adsorption capacity of cement to the DPCS polymer at 60 min is lower than that at 10 min, while the adsorption capacity of cement to the TSRS polymer at 60 min is significantly higher than that at 10 min. This phenomenon may be explained by that with the cement hydration, the DPCS molecules adsorbed on the surface particles are continuously consumed, due to the deposition of hydration products on the surface of cement particles, which decreases the number of PCs molecules in solution and decreases the adsorption capacity of cement to the DPCS polymer. conversely, with the hydration of

cement, more TSRS molecules would be released into the solution due to the hydrolysis of acrylamide in alkaline environment, which increases the number of PCs molecules in solution and increases the adsorption capacity of cement to the TSRS polymer. This also explains why the fluidity-retention ability of the TSRS polymer is better than that of DPCS polymer.

### **CRedit authorship contribution statement**

Yaqing Jiang: Conceptualization, Methodology, Investigation, Formal analysis, Writing - Original draft, Review and Editing. Tinghong Pan: Conceptualization, Methodology, Writing – Review and Editing, Supervision. Xuping Ji: Conceptualization, Methodology, Investigation, Formal analysis.

### **Declaration of competing interest**

The authors declare that they have no known competing financial interests or personal relationships that could have appeared to influence the work reported in this paper.

### **Acknowledgments**

This work was supported by the National Natural Science Foundation of China [grant numbers 51738003, 11772120].

### **References**

- [1] M.T. Souza, I.M. Ferreira, E. Guzi de Moraes, L. Senff and A.P. Novaes de Oliveira, 3D printed concrete for large-scale buildings: An overview of rheology, printing parameters, chemical admixtures, reinforcements, and economic and environmental prospects, *J. Build. Eng.* 32(2020) 101833.
- [2] J.G. Sanjayan and B. Nematollahi, 3D Concrete Printing for Construction Applications[J]. *3D Concrete Printing Technology*, 2019:1-11.
- [3] M.K. Mohan, A.V. Rahul, G. De Schutter and K. Van Tittelboom, Extrusion-based concrete 3D printing from a material perspective: A state-of-the-art review, *Cem. Concr. Compos.* 115(2021) 103855.
- [4] A. Anton, L. Reiter, T. Wangler, V. Frangez, R.J. Flatt and B. Dillenburger, A 3D

- concrete printing prefabrication platform for bespoke columns, *Autom. Constr.* 122(2021) 103467.
- [5] C. Gosselin, R. Duballet, P. Roux, N. Gaudillière, J. Dirrenberger and P. Morel, Large-scale 3D printing of ultra-high performance concrete – a new processing route for architects and builders, *Mater. Des.* 100(2016) 102-109.
- [6] H. Alhumayani, M. Gomaa, V. Soebarto and W. Jabi, Environmental assessment of large-scale 3D printing in construction: A comparative study between cob and concrete, *J. Clean. Prod.* 270(2020) 122463.
- [7] D. Heras Murcia, M. Genedy and M.M. Reda Taha, Examining the significance of infill printing pattern on the anisotropy of 3D printed concrete, *Constr. Build. Mater.* 262(2020) 120559.
- [8] I. Agustí-Juan, F. Müller, N. Hack, T. Wangler and G. Habert, Potential benefits of digital fabrication for complex structures: Environmental assessment of a robotically fabricated concrete wall, *J. Clean. Prod.* 154(2017) 330-340.
- [9] S. Muthukrishnan, S. Ramakrishnan and J. Sanjayan, Effect of microwave heating on interlayer bonding and buildability of geopolymer 3D concrete printing, *Constr. Build. Mater.* 265(2020) 120786.
- [10] J.G. Sanjayan, B. Nematollahi, M. Xia and T. Marchment, Effect of surface moisture on inter-layer strength of 3D printed concrete, *Constr. Build. Mater.* 172(2018) 468-475.
- [11] T. Marchment, J. Sanjayan and M. Xia, Method of enhancing interlayer bond strength in construction scale 3D printing with mortar by effective bond area amplification, *Mater. Des.* 169(2019) 107684.
- [12] C. Schröfl, V.N. Nerella and V. Mechtcherine, Capillary Water Intake by 3D-Printed Concrete Visualised and Quantified by Neutron Radiography, in: *First RILEM International Conference on Concrete and Digital Fabrication – Digital Concrete 2018*, 2019, 217-224.
- [13] B. Zareiyan and B. Khoshnevis, Interlayer adhesion and strength of structures in Contour Crafting - Effects of aggregate size, extrusion rate, and layer thickness, *Autom. Constr.* 81(2017) 112-121.

- [14] Y. He, X. Zhang, R.D. Hooton and X. Zhang, Effects of interface roughness and interface adhesion on new-to-old concrete bonding, *Constr. Build. Mater.* 151(2017) 582-590.
- [15] S.K. Ha, S. Na and H.K. Lee, Bond characteristics of sprayed FRP composites bonded to concrete substrate considering various concrete surface conditions, *Compos. Struct.* 100(2013) 270-279.
- [16] P.M.D. Santos and E.N.B.S. Júlio, A state-of-the-art review on roughness quantification methods for concrete surfaces, *Constr. Build. Mater.* 38(2013) 912-923.
- [17] E.N.B.S. Júlio, F.A.B. Branco and V.D. Silva, Concrete-to-concrete bond strength. Influence of the roughness of the substrate surface, *Constr. Build. Mater.* 18(2004) 675-681.
- [18] W. Mansour and S. Fayed, Effect of interfacial surface preparation technique on bond characteristics of both NSC-UHPFRC and NSC-NSC composites, *Structures.* 29(2021) 147-166.
- [19] V.N. Nerella, S. Hempel and V. Mechtcherine, Effects of layer-interface properties on mechanical performance of concrete elements produced by extrusion-based 3D-printing, *Constr. Build. Mater.* 205(2019) 586-601.
- [20] M.H. Mizan, T. Ueda and K. Matsumoto, Enhancement of the concrete-PCM interfacial bonding strength using silica fume, *Constr. Build. Mater.* 259(2020) 119774.
- [21] A. Valikhani, A.J. Jahromi, I.M. Mantawy and A. Azizinamini, Experimental evaluation of concrete-to-UHPC bond strength with correlation to surface roughness for repair application, *Constr. Build. Mater.* 238(2020) 117753.
- [22] E.N.B.S. Júlio, F.A.B. Branco, V.D. Silva and J.F. Lourenço, Influence of added concrete compressive strength on adhesion to an existing concrete substrate, *Build. Environ.* 41(2006) 1934-1939.
- [23] B. Zareiyan and B. Khoshnevis, Effects of interlocking on interlayer adhesion and strength of structures in 3D printing of concrete, *Autom. Constr.* 83(2017) 212-221.

- [24] L. Jia, F. Zhao, K. Yao and H. Du, Bond performance of repair mortar made with magnesium phosphate cement and ferroaluminate cement, *Constr. Build. Mater.* 279(2021) 122398.
- [25] L. Courard, T. Piotrowski and A. Garbacz, Near-to-surface properties affecting bond strength in concrete repair, *Cem. Concr. Compos.* 46(2014) 73-80.
- [26] C. Hu and Z. Li, Property investigation of individual phases in cementitious composites containing silica fume and fly ash, *Cem. Concr. Compos.* 57(2015) 17-26.
- [27] T.A. Soylev and R. François, Quality of steel–concrete interface and corrosion of reinforcing steel, *Cem. Concr. Res.* 33(2003) 1407-1415.
- [28] B. Panda, N.A. Noor Mohamed, S.C. Paul, G. Bhagath Singh, M.J. Tan and B. Šavija, The Effect of Material Fresh Properties and Process Parameters on Buildability and Interlayer Adhesion of 3D Printed Concrete, *Materials.* 12(2019) 2149
- [29] J.J. Assaad, Correlating thixotropy of self-consolidating concrete to stability, formwork pressure, and multilayer casting, *J. Mater. Civil. Eng.* 28(2016) 4016107.
- [30] N. Roussel and F. Cussigh, Distinct-layer casting of SCC: The mechanical consequences of thixotropy, *Cem. Concr. Res.* 38(2008) 624-632.
- [31] T. Pan, Y. Jiang, H. He, Y. Wang and K. Yin, Effect of Structural Build-Up on Interlayer Bond Strength of 3D Printed Cement Mortars, *Materials.* 14(2021) 236.
- [32] J.J. Assaad and C.A. Issa, Preliminary study on interfacial bond strength due to successive casting lifts of self-consolidating concrete – Effect of thixotropy, *Constr. Build. Mater.* 126(2016) 351-360.
- [33] T. Sivarupan, N. Balasubramani, P. Saxena, D. Nagarajan, M. El Mansori, K. Salonitis, M. Jolly and M.S. Dargusch, A review on the progress and challenges of binder jet 3D printing of sand moulds for advanced casting, *Addit. Manuf.* 40(2021) 101889.
- [34] D. Weger, A. Pierre, A. Perrot, T. Kränkel, D. Lowke and C. Gehlen, Penetration of Cement Pastes into Particle-Beds: A Comparison of Penetration Models,

- Materials. 14(2021) 389.
- [35] Y. Qian and G. De Schutter, Enhancing thixotropy of fresh cement pastes with nanoclay in presence of polycarboxylate ether superplasticizer (PCE), *Cem. Concr. Res.* 111(2018) 15-22.
- [36] S. Kawashima, M. Chaouche, D.J. Corr and S.P. Shah, Rate of thixotropic rebuilding of cement pastes modified with highly purified attapulgite clays, *Cem. Concr. Res.* 53(2013) 112-118.
- [37] Z. Zhao, M. Chen, J. Xu, L. Li, Y. Huang, L. Yang, P. Zhao and L. Lu, Mix design and rheological properties of magnesium potassium phosphate cement composites based on the 3D printing extrusion system, *Constr. Build. Mater.* 284(2021) 122797.
- [38] N. Roussel, Rheological requirements for printable concretes, *Cem. Concr. Res.* 112(2018) 76-85.
- [39] M. Chen, B. Liu, L. Li, L. Cao, Y. Huang, S. Wang, P. Zhao, L. Lu and X. Cheng, Rheological parameters, thixotropy and creep of 3D-printed calcium sulfoaluminate cement composites modified by bentonite, *Compos. Part B: Eng.* 186(2020) 107821.
- [40] C. Dai, A. Wu, Y. Qi, Z. Chen, B. Li and L. Nicolais, Mechanical Properties of Paste Slurry under Constant Shear Rate in Initial Structure Failure Process, *Adv. Mater. Sci. Eng.* 2019(2019) 2971563.
- [41] I. Ivanova and V. Mechtcherine, Effects of Volume Fraction and Surface Area of Aggregates on the Static Yield Stress and Structural Build-Up of Fresh Concrete, *Materials.* 13(2020) 1551
- [42] Q. Yuan, D. Zhou, K.H. Khayat, D. Feys and C. Shi, On the measurement of evolution of structural build-up of cement paste with time by static yield stress test vs. small amplitude oscillatory shear test, *Cem. Concr. Res.* 99(2017) 183-189.
- [43] H. Jiang, N. Jin, H. Ye, Y. Tian, X. Jin, Q. Zeng, D. Yan and X. Xu, Fractal Characterization of Non-Uniform Corrosion of Steel Bars in Concrete Beams after Accelerated depassivation and Seven-Year Natural Corrosion, *Materials.*

12(2019) 3919

- [44] B.B. Mandelbrot and B.B. Mandelbrot, *The fractal geometry of nature*, WH freeman New York, 1982.
- [45] T. Ai, R. Zhang, H.W. Zhou and J.L. Pei, Box-counting methods to directly estimate the fractal dimension of a rock surface, *Appl. Surf. Sci.* 314(2014) 610-621.
- [46] N. Roussel, G. Ovarlez, S. Garrault and C. Brumaud, The origins of thixotropy of fresh cement pastes, *Cem. Concr. Res.* 42(2012) 148-157.
- [47] J.E. Wallevik, Rheological properties of cement paste: Thixotropic behavior and structural breakdown, *Cem. Concr. Res.* 39(2009) 14-29.
- [48] J.E. Wallevik, Thixotropic investigation on cement paste: Experimental and numerical approach, *J. Non-Newton. Fluid.* 132(2005) 86-99.
- [49] J. Kruger, S. Zeranka and G. van Zijl, An ab initio approach for thixotropy characterisation of (nanoparticle-infused) 3D printable concrete, *Constr. Build. Mater.* 224(2019) 372-386.
- [50] Y. Qian, K. Lesage, K. El Cheikh and G. De Schutter, Effect of polycarboxylate ether superplasticizer (PCE) on dynamic yield stress, thixotropy and flocculation state of fresh cement pastes in consideration of the Critical Micelle Concentration (CMC), *Cem. Concr. Res.* 107(2018) 75-84.
- [51] J. Plank and B. Sachsenhauser, Experimental determination of the effective anionic charge density of polycarboxylate superplasticizers in cement pore solution, *Cem. Concr. Res.* 39(2009) 1-5.
- [52] S. Jin, J. Zhang and S. Han, Fractal analysis of relation between strength and pore structure of hardened mortar, *Constr. Build. Mater.* 135(2017) 1-7.
- [53] J. Kruger and G. van Zijl, A compendious review on lack-of-fusion in digital concrete fabrication, *Addit. Manuf.* 37(2021) 101654.
- [54] Y. Chen, K. Jansen, H. Zhang, C. Romero Rodriguez, Y. Gan, O. Çopuroğlu and E. Schlangen, Effect of printing parameters on interlayer bond strength of 3D printed limestone-calcined clay-based cementitious materials: An experimental and numerical study, *Constr. Build. Mater.* 262(2020) 120094.

- [55] H. Kloft, H. Krauss, N. Hack, E. Herrmann, S. Neudecker, P.A. Varady and D. Lowke, Influence of process parameters on the interlayer bond strength of concrete elements additive manufactured by Shotcrete 3D Printing (SC3DP), *Cem. Concr. Res.* 134(2020) 106078.
- [56] J. Van Der Putten, M. Deprez, V. Cnudde, G. De Schutter and K. Van Tittelboom, Microstructural Characterization of 3D Printed Cementitious Materials, *Materials*. 12(2019) 2993.
- [57] G. Ma, N.M. Salman, L. Wang and F. Wang, A novel additive mortar leveraging internal curing for enhancing interlayer bonding of cementitious composite for 3D printing, *Constr. Build. Mater.* 244(2020) 118305.
- [58] G.M. Moelich, J. Kruger and R. Combrinck, Plastic shrinkage cracking in 3D printed concrete, *Compos. Part B: Eng.* 200(2020) 108313.
- [59] R.J.M. Wolfs, F.P. Bos and T.A.M. Salet, Hardened properties of 3D printed concrete: The influence of process parameters on interlayer adhesion, *Cem. Concr. Res.* 119(2019) 132-140.
- [60] E. Keita, H. Bessaies-Bey, W. Zuo, P. Belin and N. Roussel, Weak bond strength between successive layers in extrusion-based additive manufacturing: measurement and physical origin, *Cem. Concr. Res.* 123(2019) 105787.
- [61] D. Liu, B. Šavija, G.E. Smith, P.E.J. Flewitt, T. Lowe and E. Schlangen, Towards understanding the influence of porosity on mechanical and fracture behaviour of quasi-brittle materials: experiments and modelling, *Int. J. Fracture*. 205(2017) 57-72.
- [62] H. Lee, J.J. Kim, J. Moon, W. Kim and E. Seo, Correlation between pore characteristics and tensile bond strength of additive manufactured mortar using X-ray computed tomography, *Constr. Build. Mater.* 226(2019) 712-720.
- [63] S. Khalilpour, E. BaniAsad and M. Dehestani, A review on concrete fracture energy and effective parameters, *Cem. Concr. Res.* 120(2019) 294-321.

Table 1. Proportion of 3D printing cement mortars.

Material	Cement	Quartz sand	Water	Nano-clay	HPMC	TSRS or DPCS polymer
Quantity(g)	1400	2100	460	11.2	3.5	4.2

Table 2. Chemical compositions of OPC (Type II) and Nc [wt.%].

Materials	CaO	SiO <sub>2</sub>	Al <sub>2</sub> O <sub>3</sub>	FeO <sub>3</sub>	Na <sub>2</sub> O	MgO	K <sub>2</sub> O	SO <sub>3</sub>	TiO <sub>2</sub>	L.O.I
OPC	62.60	21.65	5.56	4.32	0.24	0.84	0.76	2.85	-	1.27
Nc	9.62	58.4	26.73	0.51	0.21	0.20	3.05	-	0.15	1.13

Table 3. Sample with different types of superplasticizers and different printing time interval.

No.	Printing time interval (s)	Types of superplasticizers
DPCS/T20	20	DPCS
DPCS/T1800	1800	DPCS
DPCS/T3600	3600	DPCS
TSRS/T20	20	TSRS
TSRS/T1800	1800	TSRS
TSRS/T3600	3600	TSRS

Table 4. thixotropic parameters for cement mortar with DPCS polymer and TSRS polymer.

Types	$\tau_0$ (Pa)	$R_{thix}$ (Pa/s)	$t_{perc}$ (s)	$A_{thix}$ (Pa/s)
DPCS	1194	2.23	543.2	0.71
TSRS	1434	2.76	534.6	0.50

Table 5. The results of the interlayer bond strength  $f_b$  and their statistical characteristics.

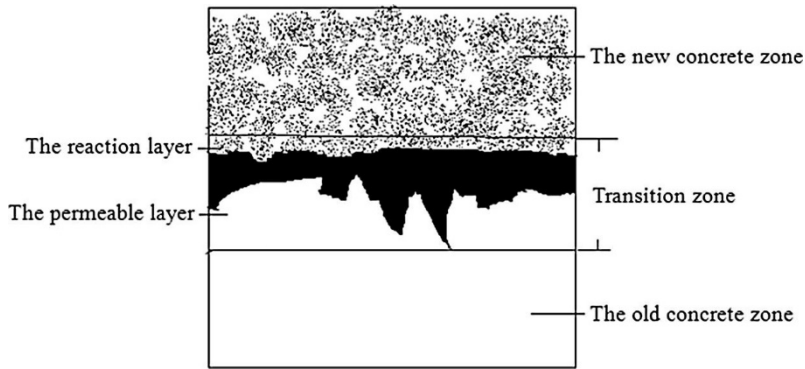
Mixtures	Testing number	Interlayer bonding strength $f_b$ (MPa)	Mean value $\bar{f}_b$ (MPa)	Standard deviation $\sigma$ (MPa)	Coefficient of variation $c_v$ %
DPCS/T20	1	1.97	1.76	0.21	11.66
	2	1.75			
	3	1.56			
DPCS/T1800	4	0.88	0.77	0.10	13.18
	5	0.75			
	6	0.68			
DPCS/T3600	7	0.48	0.39	0.09	23.07
	8	0.39			
	9	0.30			
TSRS/T20	10	2.03	1.94	0.10	4.92
	11	1.95			
	12	1.84			
TSRS/T1800	13	1.04	0.96	0.08	7.86
	14	0.95			
	15	0.89			
TSRS/T3600	16	0.59	0.55	0.05	9.62
	17	0.57			
	18	0.49			

Table B1. The molecular parameter of DPCS polymer and TSRS polymer.

Polymer	Peak Results	Mp (g/mol)	Mn (g/mol)	Mw (g/mol)	PD	Area (%)
DPCS	Peak 1	24532	19930	38993	1.956	100.00
TSRS	Peak 1	9764	7362	15373	2.088	76.02
	Peak 2	1198	860	1043	1.213	23.98

1

2



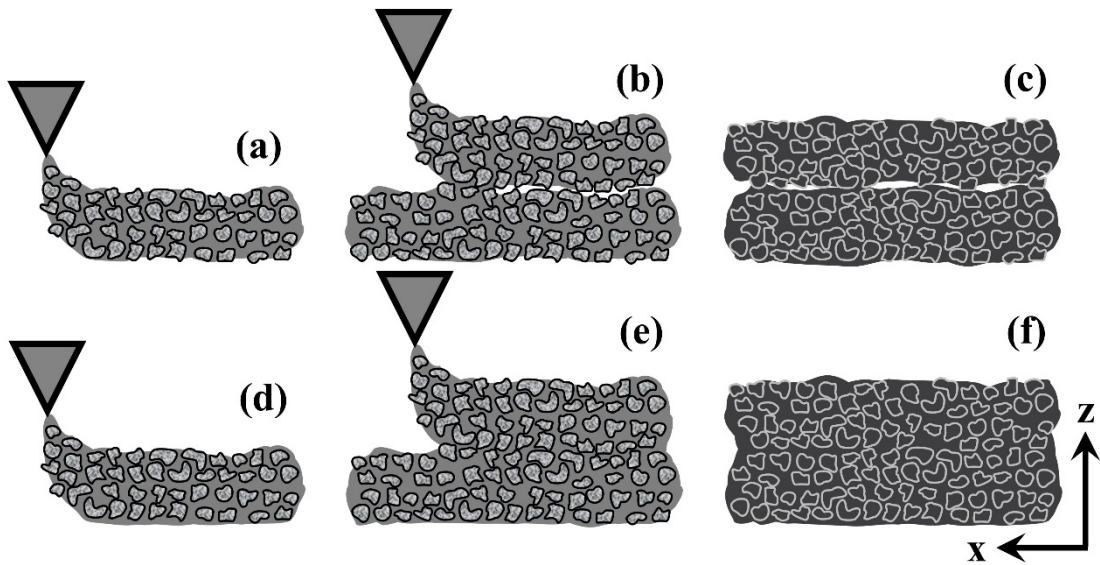
3

4

Fig. 1. The three zones-two layers model of new-to-old concrete bonding [14].

5

6



7

8

Fig. 2. Schematic diagram of spontaneous permeating of cement-based materials with complete layer bonding/filling of voids (a–c) and with incomplete layer

9

10

bonding/filling of voids (d–f).

11

12

13

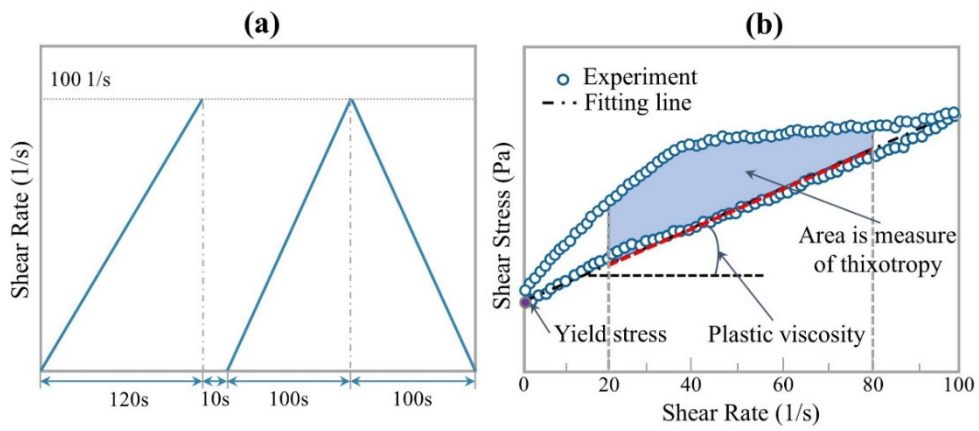
14

15

16

17

18



19

20

Fig. 3. Rheological testing protocols for thixotropic hysteresis loop.

21

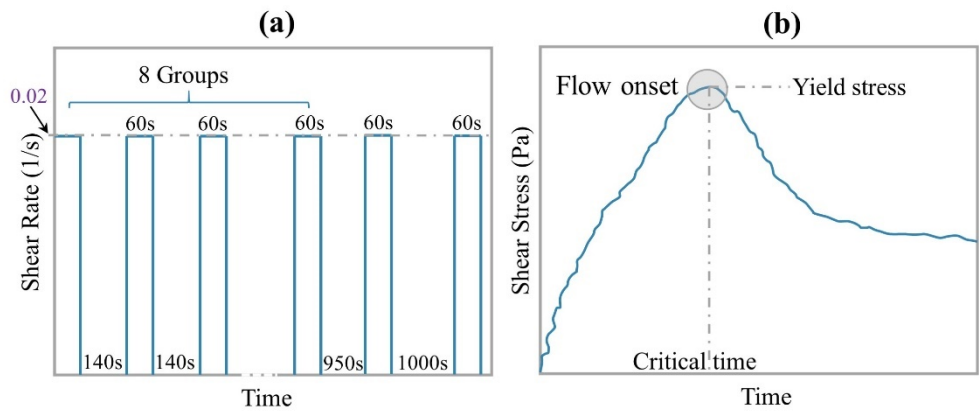
22

23

24

25

26



27

28

Fig. 4. Test protocols of static yield stress (a), and static yield stress obtained

29

from the peak value (b).

30

31

32

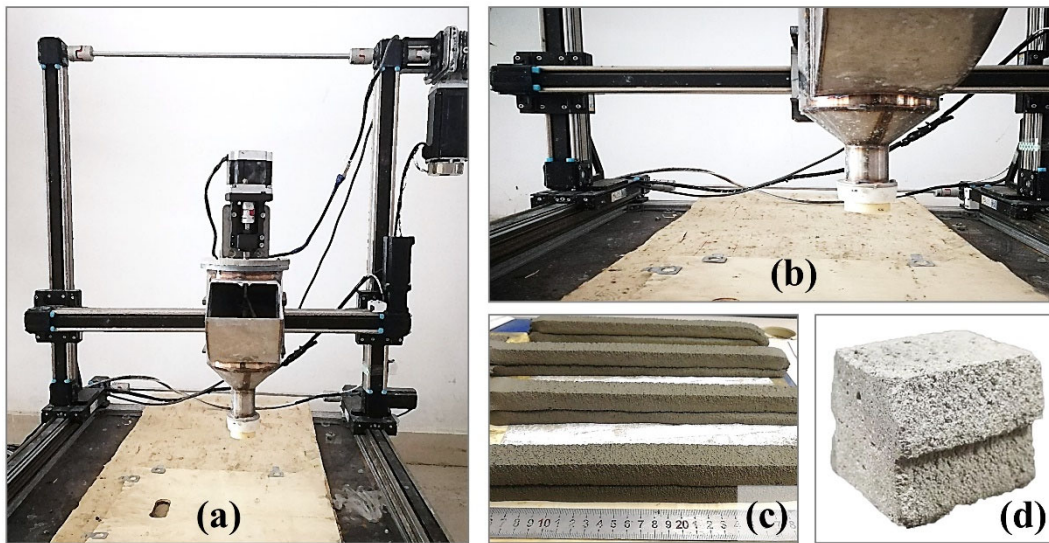
33

34

35

36

37  
38  
39  
40  
41  
42  
43  
44  
45  
46  
47

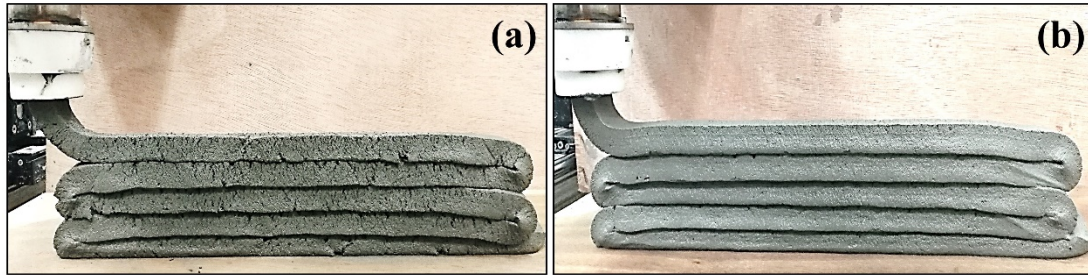


48  
49  
50  
51  
52  
53  
54  
55  
56  
57  
58

Fig. 5. 3D Printing device (a), printing nozzle (b), double-layer structures without cutting (c) and with cutting (d).

59

60



61

62

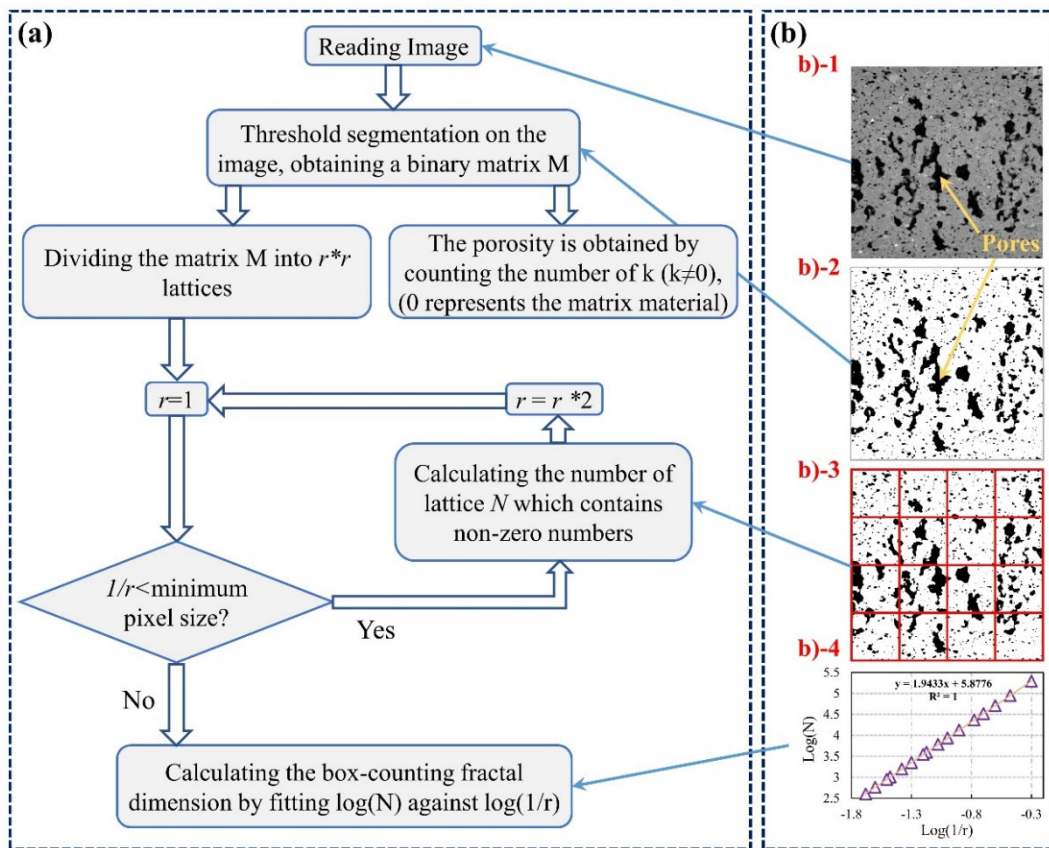
Fig. 6. Demonstration of 3D printability of mixtures: (a) DPCS/T20, (b)

63

TSRS/T20.

64

65



66

67

Fig. 7. The process of solving the plane porosity and box-counting dimension of

68

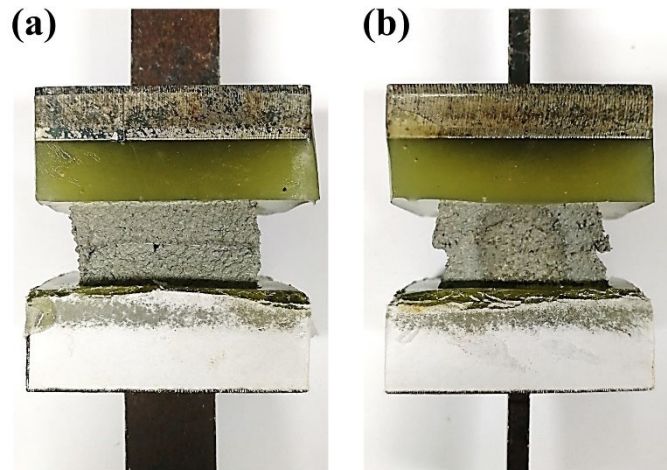
2D slice

69

70

71

72



73

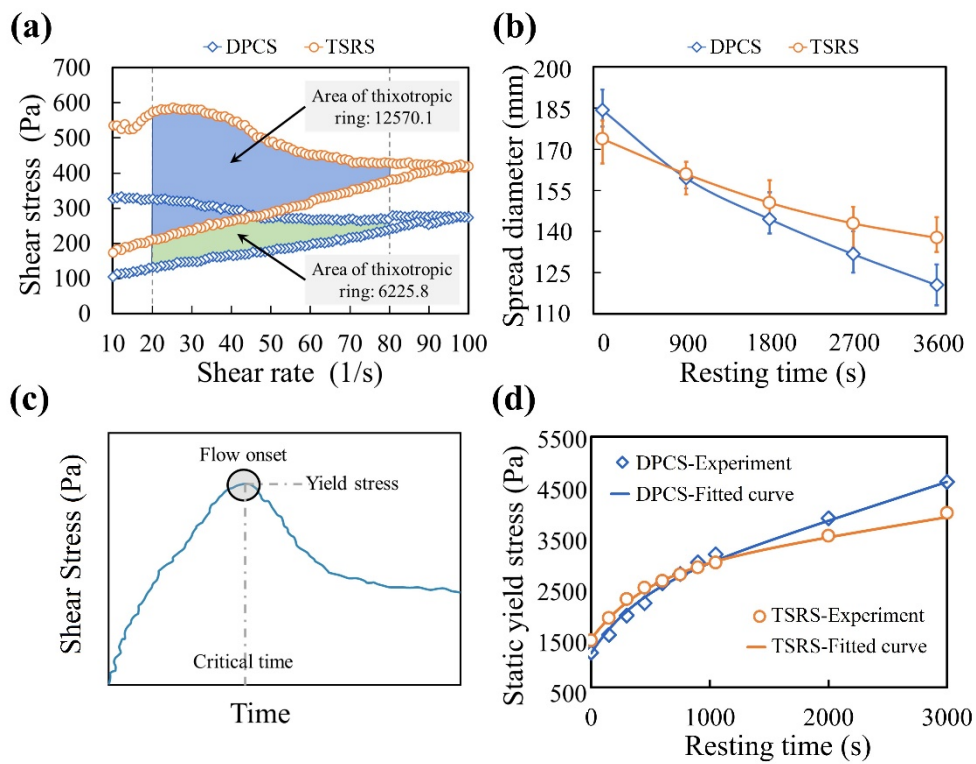
74

Fig. 8. Schematic of sample preparation for interlayer bond strength test.

75

76

77



78

79

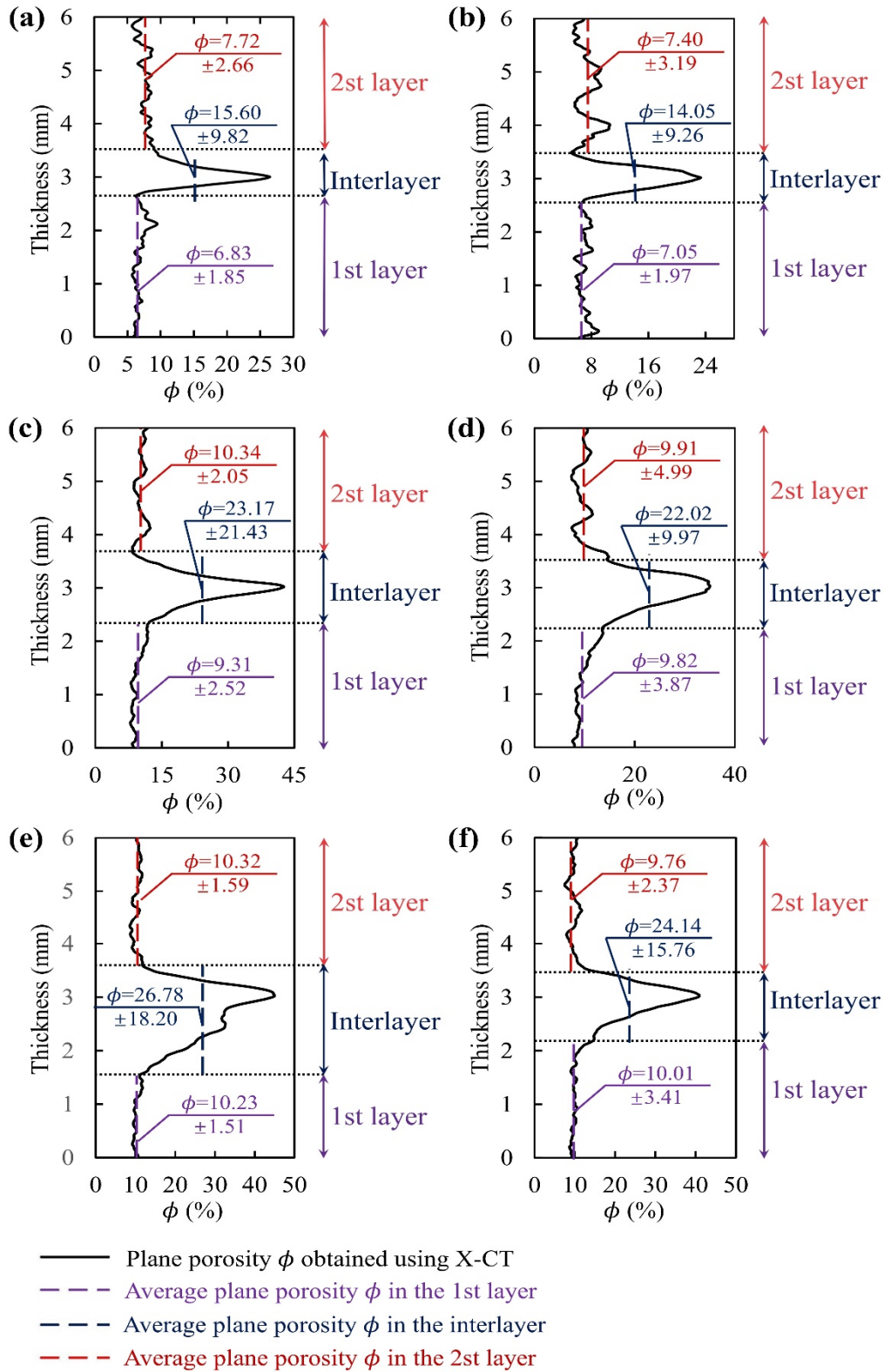
Fig. 9. The test results of thixotropic ring area (a), tripping table fluidity (b) and

80

static yield stress (d) of cement mortar.

81

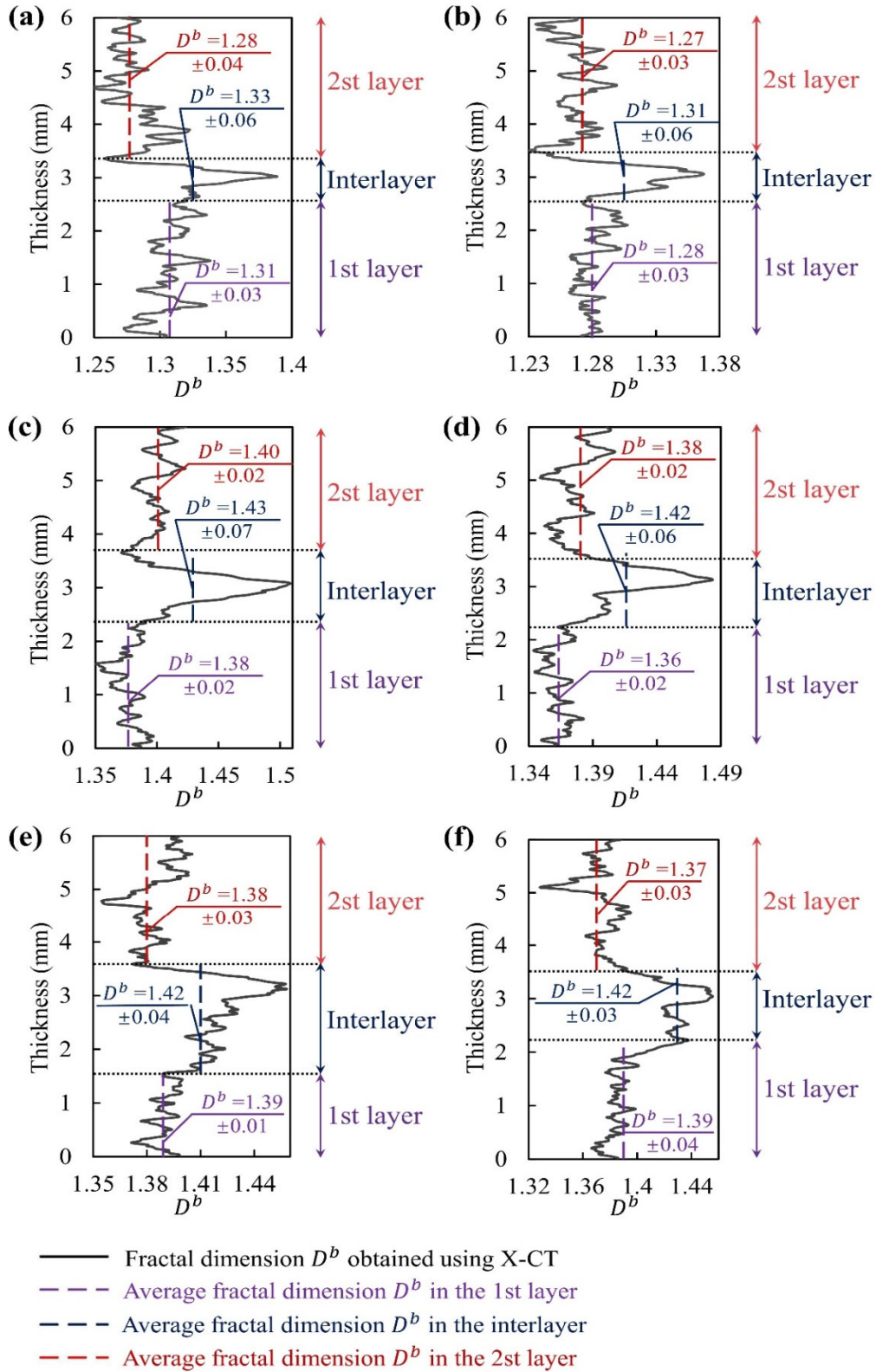
82



83

84 Fig. 10. The plane porosity  $\phi$  as a function along the thickness of printed structures  
 85 obtained on the basis of tests using the micro-CT method: (a) DPCS/T20, (b)

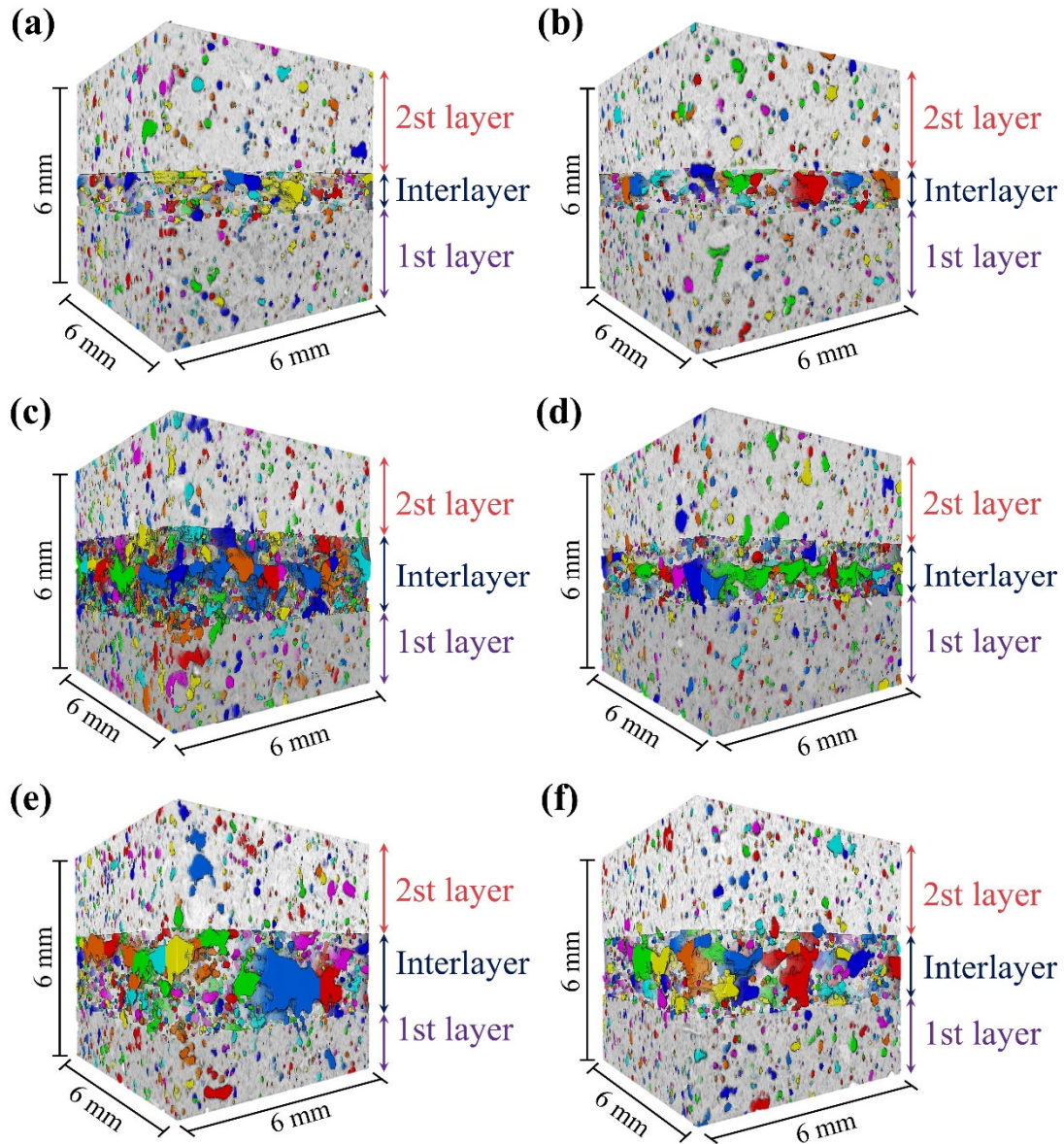
86 TSRS/T20, (c) DPCS/T1800, (d) TSRS/T1800, (a) DPCS/T3600, (b) TSRS/T3600.



87  
 88 Fig. 11. The fractal dimension  $D^b$  as a function along the thickness of printed  
 89 structures obtained on the basis of tests using the micro-CT method: (a) DPCS/T20, (b)  
 90 TSRS/T20, (c) DPCS/T1800, (d) TSRS/T1800, (a) DPCS/T3600, (b) TSRS/T3600.

91

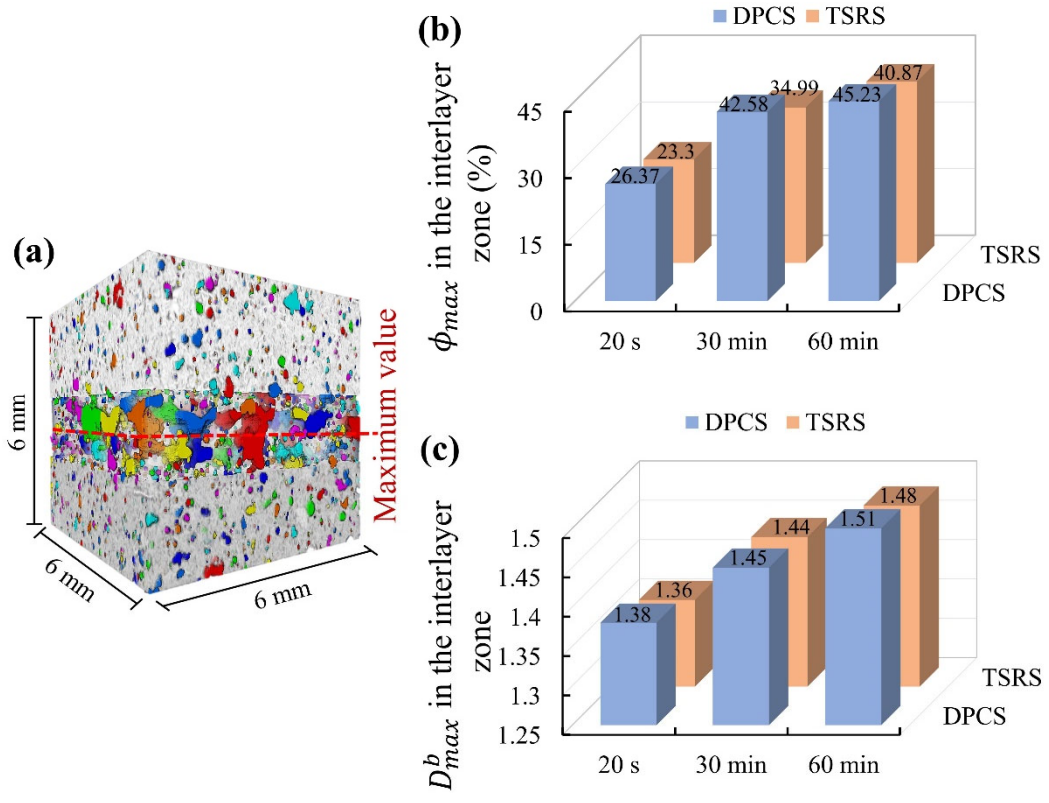
92  
93  
94



95  
96  
97  
98  
99  
100  
101  
102

Fig. 12. Reconstructions of the 3D microstructure of 3D printed structures, which were obtained on the basis of tests using the micro-CT method for samples: (a) DPCS/T20, (b) TSRS/T20, (c) DPCS/T1800, (d) TSRS/T1800, (a) DPCS/T3600, (b) TSRS/T3600.

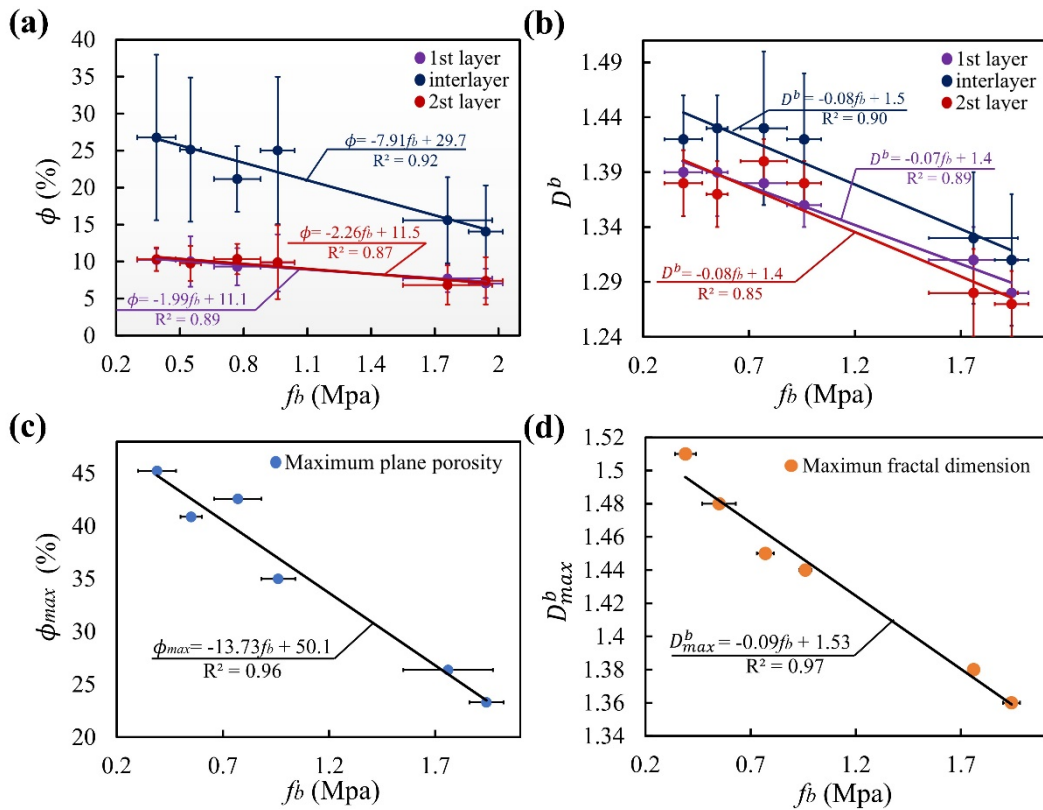
103  
 104  
 105



106  
 107  
 108  
 109  
 110  
 111  
 112  
 113  
 114  
 115  
 116  
 117  
 118  
 119  
 120

Fig. 13. Interlayer zone in the printed structures (a); The maximum value of plane porosity in the interlayer zone (b); The maximum value of fractal dimension in the interlayer zone (c).

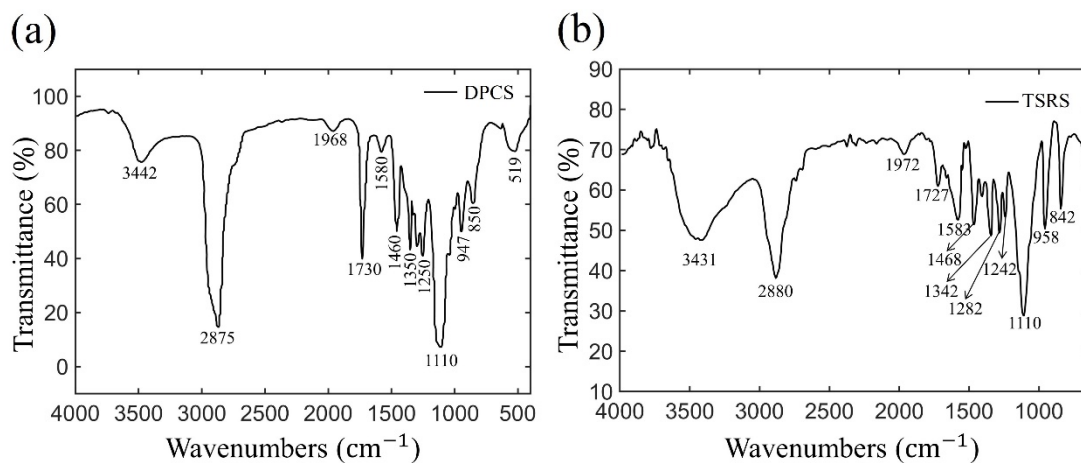
121  
 122  
 123  
 124  
 125  
 126  
 127  
 128  
 129



130  
 131  
 132  
 133  
 134  
 135  
 136  
 137

Fig. 14. The relations between the average plane porosity  $\phi$  (a), average fractal dimension  $D^b$  (b), maximum plane porosity  $\phi_{max}$  (c), maximum fractal dimension  $D^b_{max}$  (d) and the interlayer bonding strength of 3D printed structure.

138



139

140 Figure A1. FTIR spectra for DPCS and TSRS polymers.

141

142

143

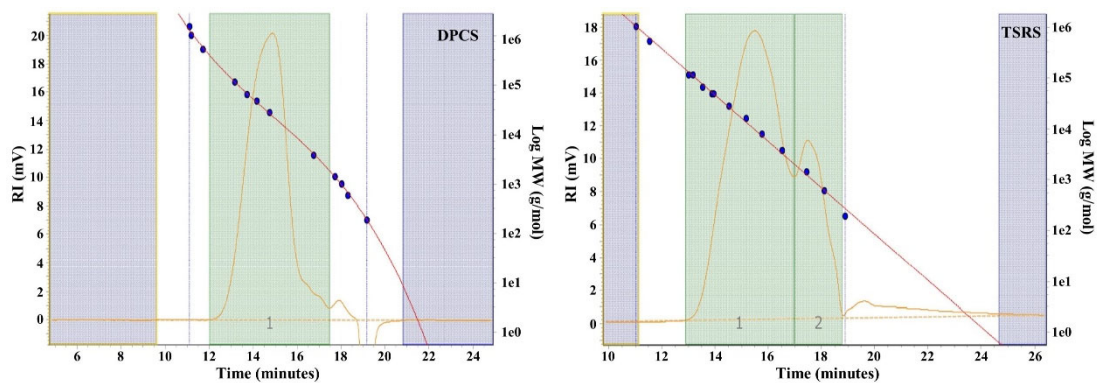
144

145

146

147

148



149

150

Figure B1. The results of GPC.

151

152

153

154

155

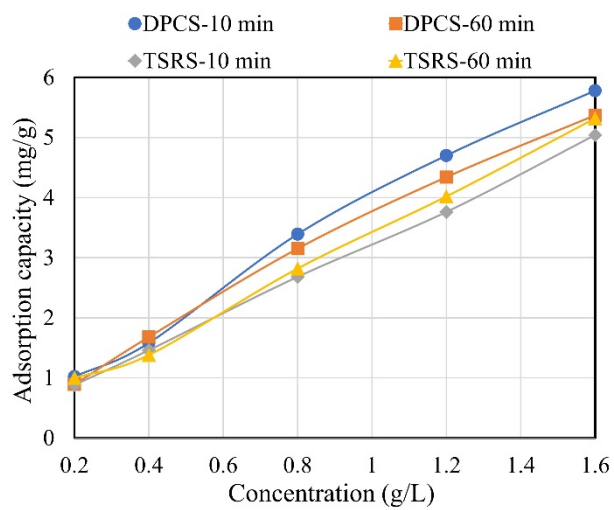
156

157

158

159

160



161

162 Figure C1. The adsorption capacity of the DPCS polymer and TSRS polymer.

163

164